Research Article Vol. 9, No. 7 / July 2021 / Photonics Research 1351

PHOTONICS Research

Directly accessing octave-spanning dissipative Kerr soliton frequency combs in an AlN microresonator

Haizhong Weng,[1,†] Jia Liu,[2,†] Adnan Ali Afridi,[1] Jing Li,[1] Jiangnan Dai,[2] Xiang Ma,[2] Yi Zhang,[2] Qiaoyin Lu,[2] John F. Donegan,[1,3] and Weihua Guo[2,4]

[1]School of Physics, CRANN and AMBER, Trinity College Dublin, Dublin 2, Ireland
[2]Wuhan National Laboratory for Optoelectronics, and School of Optical and Electronic Information, Huazhong University of Science and Technology, Wuhan 430074, China
[3]e-mail: jdonegan@tcd.ie
[4]e-mail: guow@mail.hust.edu.cn

Received 12 April 2021; revised 10 May 2021; accepted 13 May 2021; posted 13 May 2021 (Doc. ID 427567); published 1 July 2021

Self-referenced dissipative Kerr solitons (DKSs) based on optical microresonators offer prominent characteristics allowing for various applications from precision measurement to astronomical spectrometer calibration. To date, direct octave-spanning DKS generation has been achieved only in ultrahigh-*Q* silicon nitride microresonators under optimized laser tuning speed or bi-directional tuning. Here we propose a simple method to easily access the octave-spanning DKS in an aluminum nitride (AlN) microresonator. In the design, two modes that belong to different families but with the same polarization are nearly degenerate and act as a pump and an auxiliary resonance, respectively. The presence of the auxiliary resonance can balance the thermal dragging effect, crucially simplifying the DKS generation with a single pump and leading to an enhanced soliton access window. We experimentally demonstrate the long-lived DKS operation with a record single-soliton step (10.4 GHz or 83 pm) and an octave-spanning bandwidth (1100–2300 nm) through adiabatic pump tuning. Our scheme also allows for direct creation of the DKS state with high probability and without elaborate wavelength or power schemes being required to stabilize the soliton behavior.

https://doi.org/10.1364/PRJ.427567

1. INTRODUCTION

Kerr frequency comb (microcomb) generation based on parametric four-wave mixing (FWM) in monolithic microresonators with high quality (Q) factors [1], emerging as an alternative scheme, has attracted considerable interest due to miniaturization, chip-scale integration, repetition rate in the microwave and terahertz regime, and spectral coverage from visible to mid-infrared [2–5]. The recent demonstration of dissipative Kerr solitons (DKSs) [6,7], with a double balance between Kerr nonlinearity and dispersion as well as loss and parametric gain in the optical resonator, has provided a route to a fully coherent microcomb with a smooth spectral envelope and broadened width due to soliton-induced Cherenkov radiation [8,9]. The soliton microcomb has ubiquitous commercial potential for applications in dual-comb spectroscopy [10], coherent communications [11], frequency synthesizer [12], long-distance measurements [13], and quantum key distribution [14].

However, accessing soliton states in microresonators is still challenging since the DKS generation requires keeping the pump in an effective red-detuned regime, where the thermo-optic instability in the microresonator causes complex behavior [6]. Solitons have been demonstrated in MgF_2 [6], silica [15], Si_3N_4 [8,16–21], and AlN-based [22] systems. Ultrahigh nonlinearity AlGaAs microresonators with low loss were developed for the stable generation of DKSs at a cryogenic temperature [23]. Sundry techniques were adopted to demonstrate the above-mentioned solitons, including different frequency tuning schemes such as rapid forward or/and backward pump laser scans [17–19], pump modulation [21,22], and fast control of the resonator temperature [16], as well as power kicking [8]. However, the complicated control or extra equipment needed will increase the cost and limit the microcomb applications. Recently, $LiNbO_3$ has been demonstrated for accessing the perfect soliton crystal or single DKS, on-demand, due to its intrinsic photorefractive effect [24–26].

An alternative method to manipulate the power coupled into the resonance is using an auxiliary laser to pump another cavity mode, which can suppress thermal dragging dynamics during soliton formation and improve the soliton stability and access window [27–31]. However, generally for Si_3N_4

and AlN microresonators, both pump and auxiliary lasers need to be amplified to high powers with two fiber amplifiers. Moreover, a nearby auxiliary mode with cross-polarization has been proved useful to stabilize the thermal dynamics in the Si_3N_4 resonator, enabling stable access to an octave-spanning single DKS with a soliton step width of ~12 pm [18].

AlN, with a similar optical refractive index to Si_3N_4 and a large transparency window, is an ideal crystalline material for integrated photonics applications. AlN microresonators have been used to realize broadband microcombs successfully [32–34] and achieve the single Kerr soliton using the scheme of dual-pumping [30] and single-sideband modulation [22]. In addition, the strong Pockels nonlinear effect was exploited for harmonics, bi-chromatic microcomb, and Pockels quadratic soliton generation [35–37]. Nevertheless, stably accessing the Kerr soliton state with a single pump under direct tuning has not been reported for this material.

In this work, we reveal that an adjacent mode near (e.g., 35 pm longer than) the pump mode can help to mitigate the cavity thermo-optical effects, thereby allowing stable access to DKSs in an AlN microresonator via slow laser tuning. By pumping the fundamental TE (TE_{00}) mode under appropriate power, the long-lived (10.4-GHz-wide soliton step) soliton microcombs beyond an octave-spanning spectral bandwidth can be deterministically attained at a pump tuning speed of 1 nm/s. The broad soliton step allows us to directly produce the DKS with high probability by simply switching the pump wavelength from an off- to an on-resonance state. A measured 30 fs pulse trace confirms the high coherence of the soliton microcomb.

2. DEVICE CHARACTERIZATION AND PRINCIPLE

Figure 1 illustrates the device characterization and the approach taken in this work. Using standard photolithography and inductively coupled plasma etching processes [39], we fabricated the devices in a quarter of a 2 inch wafer, as shown in Fig. 1(b), that consists of a 1.2-μm-thick epitaxial single-crystal AlN film and a sapphire substrate [40]. We employed a microring resonator with a radius of 60 μm and a cross section of 2.29 μm × 1.2 μm (fully etched). The integrated bus waveguide, 500 nm apart from the resonator, is tapered from 0.91 to ~4 μm at both ends to reduce the fiber-waveguide coupling loss, which is measured to be 3.2 dB per facet. Figure 1(d) shows the measured transmission, featuring two sets of TE polarization modes, TE_{00} and TE_{10}, which are easily identified due to the different free spectral ranges (FSRs), ~374 and ~366 GHz. The resonance wavelengths of the TE_{00} and TE_{10} modes are 1550.582 and 1550.617 nm, respectively, with a separation of only 35 pm. The significantly changed extinction ratio near 1553.6 nm indicates a weak mode coupling between the two transverse modes. As fitted in Fig. 1(e), the loaded Q (Q_L) of the two nearby fundamental and first-order modes is 4.8×10^5 and 2.8×10^5, respectively. The Q_L and intrinsic Q (Q_i) of the TE_{00} mode resonant at 1562.675 nm,

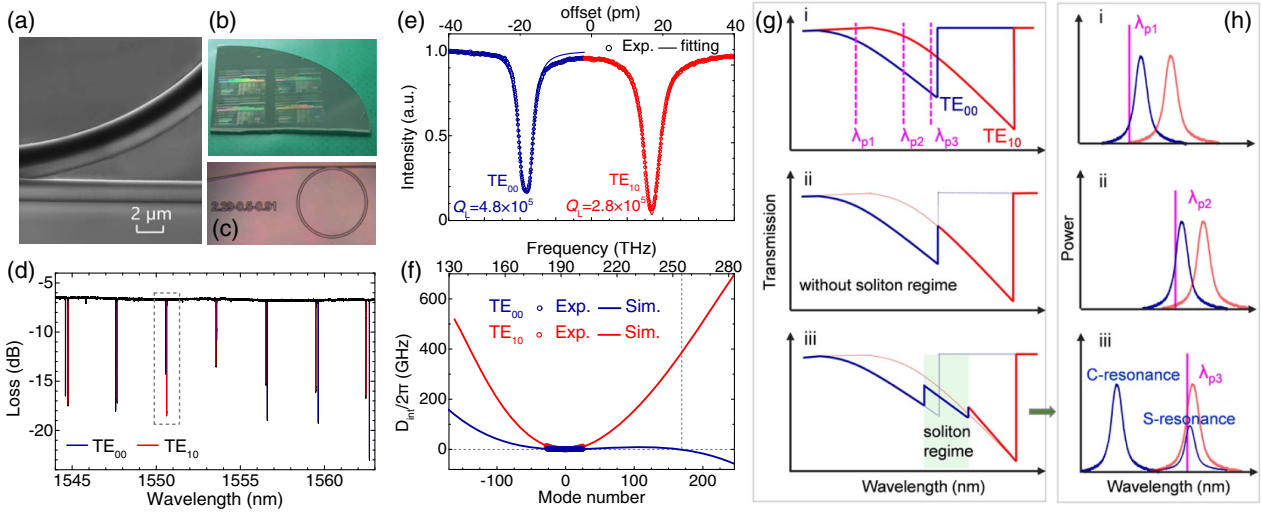

Fig. 1. (a) Scanning electron micrograph of the AlN microresonator after dry etching. (b) Photograph of a quarter of a wafer fabricated with standard photolithography. (c) Microscope image of one fabricated device. (d) Transmission spectrum of the microresonator used for octave-spanning soliton generation. (e) Zoomed-in region of the two close resonances near 1550.6 nm, with fits to determine the Q values. (f) Simulated integrated dispersion D_{int}. The circles correspond to the experimental results of around 50 resonances. (g) Schematic of the pump transmission at high power. The transmissions of TE_{00} and TE_{10} modes are plotted separately in (i), where three pump positions are marked. (ii) is the direct combination of the two resonances without achieving a soliton regime. (iii) indicates the accessible soliton under appropriate pump parameters. (h) Principle of the passive compensation of the circulating power in the microresonator by the TE_{10} resonance to achieve soliton shown in the state (iii) of (g). The laser is only coupled into TE_{00} mode at λ_{p1} (i). At λ_{p2} (ii), most of the power is coupled into the TE_{00} mode, while both modes will redshift due to the thermal effect. (iii) shows the transition into a soliton state at λ_{p3}. The sudden reduction of the pump power during the soliton generation enables the blueshift of two resonances. The pump will move to the red-detuned side of the cavity resonance, while the TE_{10} mode can compensate for the intracavity power change, thus stabilizing the soliton state. In this state, the pump resonance splits into C-resonance (cavity resonance) and S-resonance (soliton resonance) [38].

which is free from mode interactions, are extracted to be 6.1×10^5 and 1.4×10^6 considering a slightly over-coupling condition. The target geometry was chosen meticulously to ensure that the TE_{00} resonance frequency is several GHz higher than that of TE_{10} mode. For the same resonator geometry, we have observed similar behavior (two adjacent TE modes in C-band) in multiple devices, indicating that the design is easy to replicate in fabrication.

Besides the high Q, another basic requirement to yield broadband soliton microcomb is near-zero anomalous dispersion, which was also accommodated during design. The integrated dispersion D_{int} [6] was calculated and plotted in Fig. 1(f), where the center frequencies of the TE_{00} and TE_{10} modes are 193.292 and 193.289 THz, respectively. Their $D_2/2\pi$ are extracted to be 4.8 and 36.8 MHz. Both modes are in anomalous dispersion, while the TE_{00} mode has near-zero dispersion and the $D_{\text{int}} = 0$ is obtained around 255.4 THz (~1170 nm). As the schematics illustrated in Figs. 1(g) and 1(h), the TE_{10} mode can compensate for the intracavity power change and mitigate the thermal requirements to access stable soliton states.

3. EXPERIMENTAL AND SIMULATION RESULTS

A. Accessing Octave-DKS via Pump Sweeping

As the experimental setup depicted in Fig. 2, the light source (Santec TSL-710) is amplified by an erbium-doped fiber amplifier (EDFA) and injected into the waveguide through a lensed fiber. The output including transmitted pump light and generated comb lines is divided into two branches, one of which is connected with two optical spectrum analyzers (OSAs) for recording the spectra. The other branch is injected into a fiber Bragg grating (FBG) filter (bandwidth 0.4 nm) to differentiate the pump transmission (bandpass, BP) and comb lines (band rejection, BR) separately. The BR part is used for comb coherence characterization with the electrical spectrum analyzer (ESA) and autocorrelator (AC) after a photodiode (PD) and a fiber polarization controller (FPC), respectively. The BP part is sent to an oscilloscope or a powermeter for the pump transmission measurement. The powermeter with

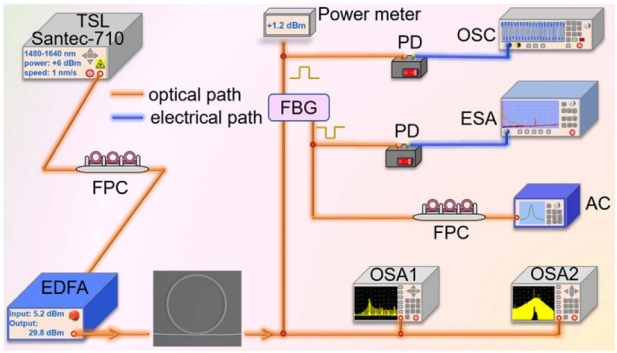

Fig. 2. Experimental setup used for single DKS generation and characterization. FPC, fiber polarization controller; EDFA, erbium-doped fiber amplifier; OSA, optical spectrum analyzer; OSA1, 600–1700 nm; OSA2, 1200–2400 nm; AC, autocorrelator; PD, photodiode; OSC, oscilloscope; ESA, electrical spectrum analyzer; FBG, fiber Bragg grating.

two synchronized channels enables the transmission measurement of all comb lines and the filtered pump at the same time.

Figure 3(a) shows the measured all and pump transmissions at 350 mW on-chip power and a pump tuning speed of 1 nm/s, as well as the calculated difference between them. A pronounced 63-pm-wide step-like structure characteristic of soliton formation is formed. The low Q factor of TE_{10} mode results in a high extinction ratio in the pump transmission, implying a strong power absorption in the cavity. By sweeping the laser wavelength to different detuning positions, we record the comb spectra and plot the evolution map in Fig. 3(b). One can observe that the spectrum changes from primary comb to modulation instability [MI, dashed line (i)] comb and solitons [dashed lines (ii) and (iii)]. The solitons exist stably when the laser wavelength ends between ~1550.78 and ~1550.84 nm, consistent with the soliton regime marked in Fig. 3(a).

The top stack of Fig. 3(c) is the generated MI comb spectrum (i), which ranges from 140 to 260 THz with a dispersive wave (DW) bump around 255 THz. Typical spectra of solitons 1 [region (ii) of Fig. 3(c)] and 2 [region (iii) of Fig. 3(c)] are presented in Fig. 3(c) subsequently, which cover an octave-spanning range from 130 to 273 THz (1100–2300 nm). The measured soliton spectra are significantly extended toward shorter wavelengths due to the emission of the DW via soliton-induced Cherenkov radiation at ~264 THz (~1136 nm). Upon further tuning the pump toward the red-sided regime before dropping out of the cavity resonance, we can only observe a few weak sidebands (state iv) generated from the TE_{10} mode due to the lower Q factor and larger dispersion. Therefore, our geometry design is ideal for generating the DKSs without any concern about the nonlinear competition between the two transverse modes.

We also observed the shiny green light emission during the soliton formation [see insets in Fig. 3(c)], corresponding to the third-harmonic generation (THG) at ~580 THz. We believe the other weak spectrum bump occurrence around 290 THz arises from the THG and the optical parametric oscillation [37]. The soliton centroids are 5.2 and 7.4 THz lower than the pump because of the Raman self-frequency shift effect and the DW recoil [41–43]. By fitting the spectral with sech^2 function, we can find the full widths at half-maximum (FWHMs) of solitons 1 and 2 are 15.2 and 12.3 THz, corresponding to 40 and 33 modes, respectively. Their minimum transform-limited pulse width τ is estimated to be 21 and 26 fs, using 0.315 × the pulse FWHM where the pulse shape is sech^2 [6].

The transition from the MI comb to the soliton comb is verified by the drastic reduction of low-frequency intensity noise [see Fig. 3(d)]. To further confirm the single DKS states, the temporal characteristics were also carried out through the second-harmonic generation (SHG)-based autocorrelation measurement. Figure 3(e) shows the measured soliton autocorrelation trace, which has a poor signal-to-noise ratio (SNR) since the soliton comb power is at the limit that can be detected by the AC. However, the pulses are clearly separated by ~2.66 ps, inversely proportional to the FSR of ~374 GHz. Within a narrow measurement range, an extremely narrow pulse [see Fig. 3(f)] with ~30 fs width and improved SNR can be obtained based on the sech^2 fitting. The measured pulse

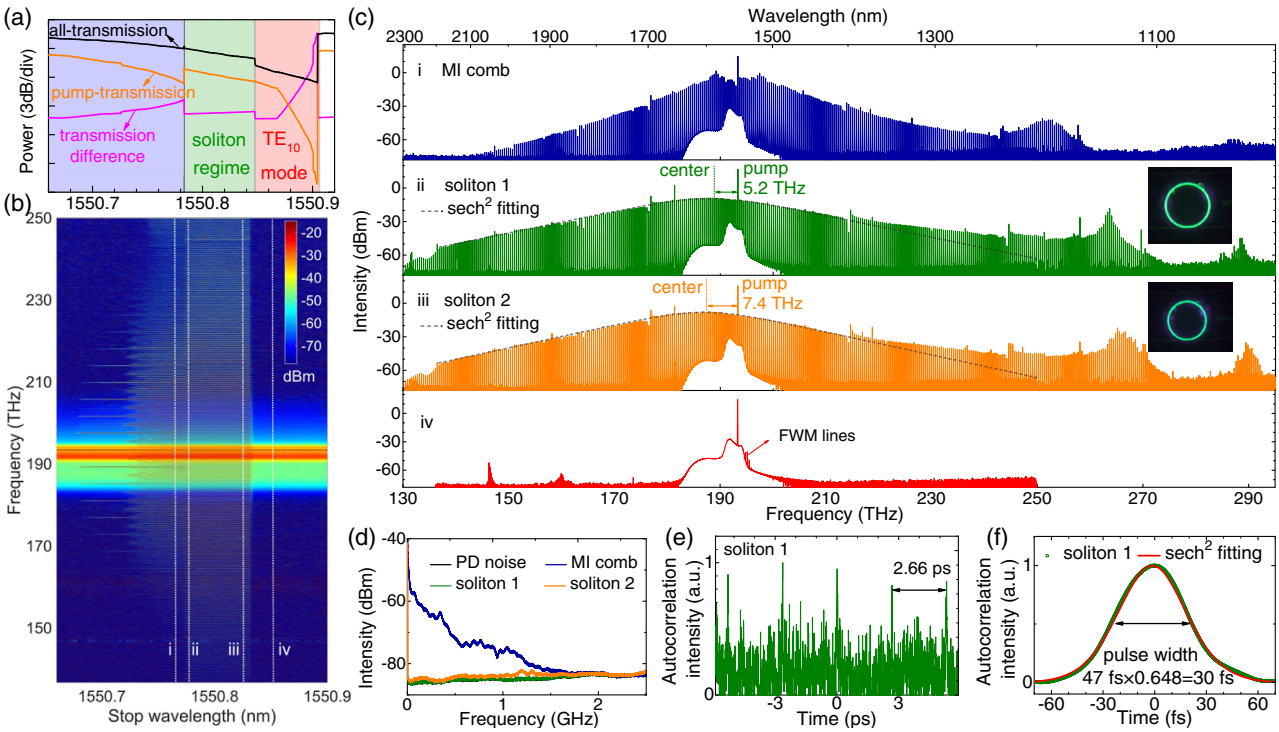

Fig. 3. (a) Resonance transmissions at an on-chip power of 350 mW and a pump tuning speed of 1 nm/s. (b) Frequency comb evolution map. (c) Optical spectral snapshots of different comb states, corresponding to the dash lines in (b). The dashed lines show the fitted sech^2 envelope. Insets are the microscope images of the green light emission from the microresonator. (d) Low-frequency intensity noise of the microcombs and the PD noise floor. (e) SHG-based autocorrelation measurement for the soliton 1 state. (f) A single pulse with sech^2 fitting, where the trace FWHM needs to be multiplied by 0.648 to yield the real pulse width.

width is larger than that estimated from the spectrum (21 fs) due to the limited responsivity beyond ~1600 nm of the AC.

To explore the dependence of soliton existence range on the pump power, we characterized the all and pump transmissions, under various powers, and we plot their difference in Fig. 4. A striking soliton step with 10.4 GHz (83 pm) width is observed at 335 mW, which is the widest soliton existence window as far as we know. When further increasing the power, the soliton step declines nearly linearly (~ −0.1 GHz/mW) and disappears at 440 mW due to the residual thermal effects. It should be noted that the soliton existence range can be further increased to ~90 pm when we use a simple, slow laser piezo tuning (several GHz/s, by hand). The soliton states are sustained for 2 h at an on-chip power of ~410 mW.

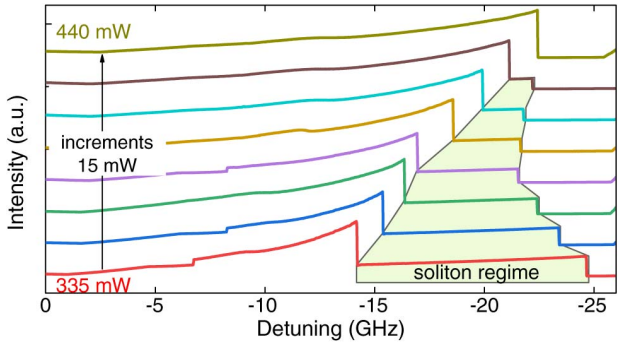

Fig. 4. Power difference between all and pump transmissions measured at on-chip powers with a laser tuning speed of 1 nm/s. The green polygon indicates the soliton existence regime.

B. Accessing Octave-DKS by Tuning the Pump Wavelength with One Step

One highlight of our system is the direct creation of the DKS state by simply red tuning the pump light with one step, thereby eliminating the requirement for complex pump tuning or power kicking techniques. As the schematic depicted in Fig. 5(a), the laser wavelength was switched 50 times between an off- (λ_{start}) and an on-resonance (λ_{stop}) state. The duration of each wavelength is 2 s.

The possibility of accessible soliton versus the λ_{start} and λ_{stop} was recorded and depicted in Fig. 5(b), as confirmed by monitoring the microcomb spectrum and pump transmission with both OSA and real-time oscilloscope. We can directly access the soliton with high probability, over 80% when the λ_{stop} is 1550.720 or 1550.730 nm and the step values locate between 0.09 and 0.12 nm. Compared with the soliton existence regime (1550.781–1550.844 nm) marked in Fig. 3(a), we note that tuning the pump wavelength with step mode will reduce the thermal effects within the microresonator, thus decreasing the detuning required for soliton generation. Figure 5(c) plot the measured pump transmission when the λ_{start} and λ_{stop} are 1550.620 and 1550.720 nm, 1550.630 and 1550.730 nm, and 1550.640 and 1550.740 nm, respectively, with a fixed step of 0.1 nm. The successful and failed (accessible and inaccessible to the soliton states) attempts are

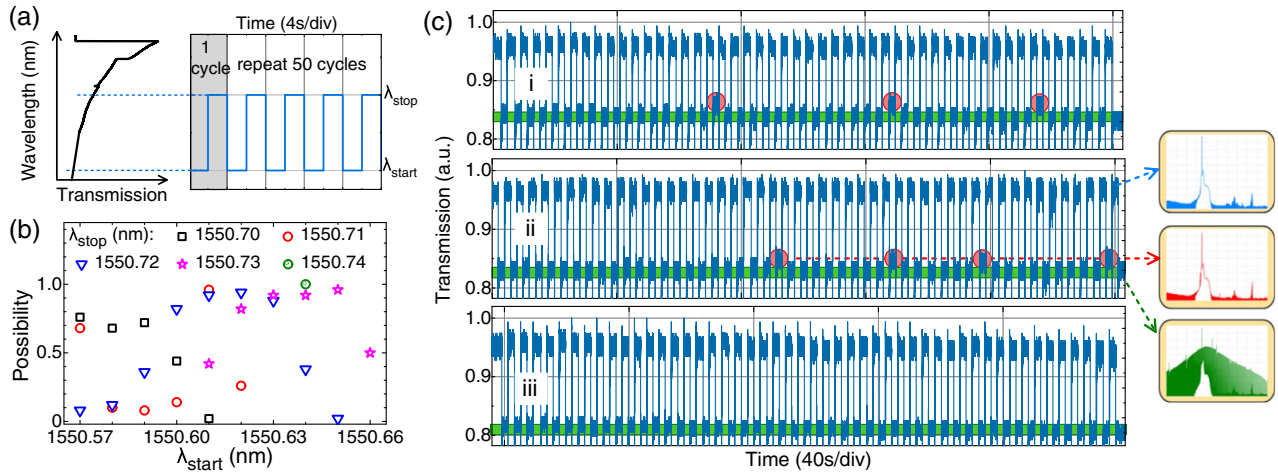

Fig. 5. (a) Schematic of the laser wavelength tuning with step mode. (b) Soliton accessing possibility among 50 attempts, versus the λ_{start} and λ_{stop}. (c) Record pump transmission traces when $\lambda_{start}/\lambda_{stop}$ are (i) 1550.620/1550.720 nm, (ii) 1550.630/1550.730 nm, and (iii) 1550.640/1550.740 nm, respectively. Green rectangles and red circles indicate the successful and failed attempts, respectively.

marked by green rectangles and red circles. The success rate is as high as 94%, 92%, and even 100%, respectively.

4. DISCUSSION

As investigated in Refs. [18,20], with an auxiliary mode, the intracavity power is modified such that a part of the soliton regime becomes thermally stable. Therefore, the soliton behavior is affected by the mode separation and a thermally induced cavity redshift, which is related to the pump power, the mode Q factors of the two adjacent modes, and thermal conductance of the microresonator. The influences of these parameters on the soliton dynamics in our single-crystalline AlN microresonators need further study in both numerical and experimental investigations.

To increase the overall yield for ensuring the pump and auxiliary modes are close, we will design and fabricate microresonators with minor changes around the target parameters by taking the fabrication variation into account. A patterned metal contact can be deposited near the devices for attempting to fine-tune the mode separation and coupling. This provides another dimension, together with optimized pump tuning speed and power, to control the thermal effect for accessing soliton states more easily. We can estimate that the pump power required for soliton generation can be decreased to tens of mW assuming the intrinsic Q factor was increased to 10 million, which is needed to directly generate the soliton by pumping the passive microresonator with a laser diode chip. Moreover, instead of the mixed polarization of pump and auxiliary modes [18], the same polarization scheme eliminates the need for an in-line polarization controller for realizing the vision of hybrid integration. By designing different radii and resonator widths, one can also expect the soliton microcombs with different repetition rates in different materials by pumping at other wavelength windows such as 1300 and 1064 nm.

Table 1. Comparison of Single Kerr Solitons Generated with Various Chip-Integrated Microresonators

Material	FSR (GHz)	Q_i	On-Chip Power (mW)	Spectral Range (nm)	Tuning Method	Soliton Step	Reference
Si_3N_4	200	–	71	1470–1620	Thermally tuned resonance	–	[16]
Si_3N_4	230	1.4×10^6[a]	200	1400–1700	Forward and backward tuning	–	[17]
Si_3N_4	1000	2×10^6	120 ± 15	1100–2320[b]	Forward sweeping, 0.8 nm/s	~12 pm	[18]
Si_3N_4	1000	1×10^6[a]	455	1100–2300[b]	Forward and backward tuning	–	[19]
Si_3N_4	99	15×10^6	6.2	1540–1620	Piezo laser tuning		[44]
Si_3N_4	40	16×10^6	30	1520–1600	Turn-key soliton		[45]
$LiNbO_3$	199.7	2.2×10^6[a]	33	1470–1650	Forward or backward sweeping	~0.5 GHz	[24]
$LiNbO_3$	335	1×10^6	240	1190–2140	Backward sweeping, −0.5 nm/s	~0.5 GHz	[25]
AlN	225	2.4×10^6	~1000	1400–1700	Forward sweeping, 20 nm/s	0.2 pm	[30]
AlN	433	1.6×10^6	~390	1050–2400[b]	Single-sideband modulation, forward sweeping 60 pm/μs and backward tuning	–	[46]
AlN	374	1.4×10^6	~335	1100–2300[b]	Forward sweeping, 1 nm/s, or manually tuning, or step mode	~83 pm, ~10.4 GHz	This work

[a]Represents the loaded Q.
[b]Represents the octave-spanning spectral range.

5. CONCLUSION

A simple route is proposed and demonstrated to stably achieve the octave-spanning DKS in an AlN microresonator, in which a nearby auxiliary mode is slightly red-detuned from the pump mode. The auxiliary resonance can compensate for the intracavity power change and balance the thermal effects in the resonator, thus producing and broadening the soliton step significantly. A comparison of different nonlinear material platforms for single soliton generation is shown in Table 1. In this work, an octave-spanning soliton microcomb ranging from 130 to 273 THz, with a repetition rate of ~374 GHz, is first demonstrated in AlN with a single pump under direct wavelength tuning. The spectral bandwidth is at a similar level to that realized with the state-of-the-art Si_3N_4 technology, while more comb lines are expected in our AlN microresonators due to the smaller repetition rate. Moreover, the demonstrated 10.4 GHz-wide single soliton step is, to the best of our knowledge, the widest soliton accessing window so far, which is enhanced by ~7 times compared with the soliton step demonstrated in Si_3N_4 microresonator [18]. Benefiting from this, we can directly reach the soliton states with high probability by controlling the pump wavelength with step mode, which will relax the strict requirements in controlling the pump or the cavity temperature. The free-noise at low frequency and 30 fs soliton pulse trace confirm the high coherence of the generated solitons. We believe such a deterministic and simplified approach for accessing soliton states is critical for chip-based self-referenced microcombs and their potential applications outside the laboratory.

Funding. Science Foundation Ireland (17/NSFC/4918); National Natural Science Foundation of China (61861136001).

Acknowledgment. The authors would like to thank Prof. Liam Barry for the technical assistance.

Disclosures. The authors declare no conflicts of interest.

Data Availability. Data underlying the results presented in this paper are not publicly available at this time but may be obtained from the authors upon reasonable request.

†These authors contributed equally to this paper.

REFERENCES

1. P. Del'Haye, A. Schliesser, O. Arcizet, T. Wilken, R. Holzwarth, and T. J. Kippenberg, "Optical frequency comb generation from a monolithic microresonator," Nature **450**, 1214–1217 (2007).
2. J. S. Levy, A. Gondarenko, M. A. Foster, A. C. Turner-Foster, A. L. Gaeta, and M. Lipson, "CMOS-compatible multiple-wavelength oscillator for on-chip optical interconnects," Nat. Photonics **4**, 37–40 (2010).
3. A. G. Griffith, R. K. W. Lau, J. Cardenas, Y. Okawachi, A. Mohanty, R. Fain, Y. H. D. Lee, M. Yu, C. T. Phare, C. B. Poitras, A. L. Gaeta, and M. Lipson, "Silicon-chip mid-infrared frequency comb generation," Nat. Commun. **6**, 6299 (2015).
4. M. Karpov, M. H. P. Pfeiffer, J. Liu, A. Lukashchuk, and T. J. Kippenberg, "Photonic chip-based soliton frequency combs covering the biological imaging window," Nat. Commun. **9**, 1146 (2018).
5. J. Ma, L. Xiao, J. Gu, H. Li, X. Cheng, G. He, X. Jiang, and M. Xiao, "Visible Kerr comb generation in a high-Q silica microdisk resonator with a large wedge angle," Photon. Res. **7**, 573–578 (2019).
6. T. Herr, V. Brasch, J. D. Jost, C. Y. Wang, N. M. Kondratiev, M. L. Gorodetsky, and T. J. Kippenberg, "Temporal solitons in optical microresonators," Nat. Photonics **8**, 145–152 (2014).
7. W. Wang, L. Wang, and W. Zhang, "Advances in soliton microcomb generation," Adv. Photon. **2**, 034001 (2020).
8. V. Brasch, M. Geiselmann, T. Herr, G. Lihachev, M. H. P. Pfeiffer, M. L. Gorodetsky, and T. J. Kippenberg, "Photonic chip–based optical frequency comb using soliton Cherenkov radiation," Science **351**, 357–360 (2016).
9. T. J. Kippenberg, A. L. Gaeta, M. Lipson, and M. L. Gorodetsky, "Dissipative Kerr solitons in optical microresonators," Science **361**, eaan8083 (2018).
10. M.-G. Suh, Q.-F. Yang, K. Y. Yang, X. Yi, and K. J. Vahala, "Microresonator soliton dual-comb spectroscopy," Science **354**, 600–603 (2016).
11. P. Marin-Palomo, J. N. Kemal, M. Karpov, A. Kordts, J. Pfeifle, M. H. P. Pfeiffer, P. Trocha, S. Wolf, V. Brasch, M. H. Anderson, R. Rosenberger, K. Vijayan, W. Freude, T. J. Kippenberg, and C. Koos, "Microresonator-based solitons for massively parallel coherent optical communications," Nature **546**, 274–279 (2017).
12. D. T. Spencer, T. Drake, T. C. Briles, J. Stone, L. C. Sinclair, C. Fredrick, Q. Li, D. Westly, B. R. Ilic, A. Bluestone, N. Volet, T. Komljenovic, L. Chang, S. H. Lee, D. Y. Oh, M.-G. Suh, K. Y. Yang, M. H. P. Pfeiffer, T. J. Kippenberg, E. Norberg, L. Theogarajan, K. Vahala, N. R. Newbury, K. Srinivasan, J. E. Bowers, S. A. Diddams, and S. B. Papp, "An optical-frequency synthesizer using integrated photonics," Nature **557**, 81–85 (2018).
13. J. Wang, Z. Lu, W. Wang, F. Zhang, J. Chen, Y. Wang, X. Zhao, J. Zheng, S. T. Chu, W. Zhao, B. E. Little, X. Qu, and W. Zhang, "Long distance ranging with high precision using a soliton microcomb," Photon. Res. **8**, 1964–1972 (2020).
14. F.-X. Wang, W. Wang, R. Niu, X. Wang, C.-L. Zou, C.-H. Dong, B. E. Little, S. T. Chu, H. Liu, P. Hao, S. Liu, S. Wang, Z.-Q. Yin, D.-Y. He, W. Zhang, W. Zhao, Z.-F. Han, G.-C. Guo, and W. Chen, "Quantum key distribution with on-chip dissipative Kerr soliton," Laser Photon. Rev. **14**, 1900190 (2020).
15. X. Yi, Q.-F. Yang, K. Y. Yang, M.-G. Suh, and K. Vahala, "Soliton frequency comb at microwave rates in a high-Q silica microresonator," Optica **2**, 1078–1085 (2015).
16. C. Joshi, J. K. Jang, K. Luke, X. Ji, S. A. Miller, A. Klenner, Y. Okawachi, M. Lipson, and A. L. Gaeta, "Thermally controlled comb generation and soliton modelocking in microresonators," Opt. Lett. **41**, 2565–2568 (2016).
17. C. Bao, Y. Xuan, J. A. Jaramillo-Villegas, D. E. Leaird, M. Qi, and A. M. Weiner, "Direct soliton generation in microresonators," Opt. Lett. **42**, 2519–2522 (2017).
18. Q. Li, T. C. Briles, D. A. Westly, T. E. Drake, J. R. Stone, B. R. Ilic, S. A. Diddams, S. B. Papp, and K. Srinivasan, "Stably accessing octave-spanning microresonator frequency combs in the soliton regime," Optica **4**, 193–203 (2017).
19. M. H. P. Pfeiffer, C. Herkommer, J. Liu, H. Guo, M. Karpov, E. Lucas, M. Zervas, and T. J. Kippenberg, "Octave-spanning dissipative Kerr soliton frequency combs in Si_3N_4 microresonators," Optica **4**, 684–691 (2017).
20. T. Wildi, V. Brasch, J. Liu, T. J. Kippenberg, and T. Herr, "Thermally stable access to microresonator solitons via slow pump modulation," Opt. Lett. **44**, 4447–4450 (2019).
21. S. Wan, R. Niu, Z.-Y. Wang, J.-L. Peng, M. Li, J. Li, G.-C. Guo, C.-L. Zou, and C.-H. Dong, "Frequency stabilization and tuning of breathing solitons in Si_3N_4 microresonators," Photon. Res. **8**, 1342–1349 (2020).
22. Z. Gong, A. Bruch, M. Shen, X. Guo, H. Jung, L. Fan, X. Liu, L. Zhang, J. Wang, J. Li, J. Yan, and H. X. Tang, "High-fidelity cavity soliton generation in crystalline AlN micro-ring resonators," Opt. Lett. **43**, 4366–4369 (2018).
23. G. Moille, L. Chang, W. Xie, A. Rao, X. Lu, M. Davanço, J. E. Bowers, and K. Srinivasan, "Dissipative Kerr solitons in a III-V microresonator," Laser Photon. Rev. **14**, 2000022 (2020).

24. Y. He, Q.-F. Yang, J. Ling, R. Luo, H. Liang, M. Li, B. Shen, H. Wang, K. Vahala, and Q. Lin, "Self-starting bi-chromatic $LiNbO_3$ soliton microcomb," Optica **6**, 1138–1144 (2019).
25. Z. Gong, X. Liu, Y. Xu, and H. X. Tang, "Near-octave lithium niobate soliton microcomb," Optica **7**, 1275–1278 (2020).
26. Y. He, J. Ling, M. Li, and Q. Lin, "Perfect soliton crystals on demand," Laser Photon. Rev. **14**, 1900339 (2020).
27. Z. Lu, W. Wang, W. Zhang, S. T. Chu, B. E. Little, M. Liu, L. Wang, C.-L. Zou, C.-H. Dong, B. Zhao, and W. Zhao, "Deterministic generation and switching of dissipative Kerr soliton in a thermally controlled micro-resonator," AIP Adv. **9**, 025314 (2019).
28. S. Zhang, J. M. Silver, L. Del Bino, F. Copie, M. T. M. Woodley, G. N. Ghalanos, A. Ø. Svela, N. Moroney, and P. Del'Haye, "Sub-milliwatt-level microresonator solitons with extended access range using an auxiliary laser," Optica **6**, 206–212 (2019).
29. H. Zhou, Y. Geng, W. Cui, S.-W. Huang, Q. Zhou, K. Qiu, and C. W. Wong, "Soliton bursts and deterministic dissipative Kerr soliton generation in auxiliary-assisted microcavities," Light Sci. Appl. **8**, 50 (2019).
30. Y. Zheng, C. Sun, B. Xiong, L. Wang, J. Wang, Y. Han, Z. Hao, H. Li, J. Yu, Y. Luo, J. Yan, T. Wei, Y. Zhang, and J. Wang, "Soliton comb generation in air-clad AlN microresonators," in *Conference on Lasers and Electro-Optics* (Optical Society of America, 2020), paper SW4J.3.
31. X. Wang, P. Xie, W. Wang, Y. Wang, Z. Lu, L. Wang, S. T. Chu, B. E. Little, W. Zhao, and W. Zhang, "Program-controlled single soliton microcomb source," Photon. Res. **9**, 66–72 (2020).
32. H. Jung, C. Xiong, K. Y. Fong, X. Zhang, and H. X. Tang, "Optical frequency comb generation from aluminum nitride microring resonator," Opt. Lett. **38**, 2810–2813 (2013).
33. X. Liu, C. Sun, B. Xiong, L. Wang, J. Wang, Y. Han, Z. Hao, H. Li, Y. Luo, J. Yan, T. Wei, Y. Zhang, and J. Wang, "Integrated high-*Q* crystalline AlN microresonators for broadband Kerr and Raman frequency combs," ACS Photon. **5**, 1943–1950 (2018).
34. H. Weng, J. Liu, A. A. Afridi, J. Li, J. Dai, X. Ma, Y. Zhang, Q. Lu, J. F. Donegan, and W. Guo, "Octave-spanning Kerr frequency comb generation with stimulated Raman scattering in an AlN microresonator," Opt. Lett. **46**, 540–543 (2021).
35. H. Jung, R. Stoll, X. Guo, D. Fischer, and H. X. Tang, "Green, red, and IR frequency comb line generation from single IR pump in AlN microring resonator," Optica **1**, 396–399 (2014).
36. X. Liu, C. Sun, B. Xiong, L. Wang, J. Wang, Y. Han, Z. Hao, H. Li, Y. Luo, J. Yan, T. Wei, Y. Zhang, and J. Wang, "Generation of multiple near-visible comb lines in an AlN microring via $\chi^{(2)}$ and $\chi^{(3)}$ optical nonlinearities," Appl. Phys. Lett. **113**, 171106 (2018).
37. A. W. Bruch, X. Liu, Z. Gong, J. B. Surya, M. Li, C.-L. Zou, and H. X. Tang, "Pockels soliton microcomb," Nat. Photonics **15**, 21–27 (2021).
38. H. Guo, M. Karpov, E. Lucas, A. Kordts, M. H. P. Pfeiffer, V. Brasch, G. Lihachev, V. E. Lobanov, M. L. Gorodetsky, and T. J. Kippenberg, "Universal dynamics and deterministic switching of dissipative Kerr solitons in optical microresonators," Nat. Phys. **13**, 94–102 (2017).
39. J. Liu, H. Weng, A. A. Afridi, J. Li, J. Dai, X. Ma, H. Long, Y. Zhang, Q. Lu, J. F. Donegan, and W. Guo, "Photolithography allows high-Q AlN microresonators for near octave-spanning frequency comb and harmonic generation," Opt. Express **28**, 19270–19280 (2020).
40. Y. Zhang, H. Long, J. Zhang, B. Tan, Q. Chen, S. Zhang, M. Shan, Z. Zheng, J. Dai, and C. Chen, "Fast growth of high quality AlN films on sapphire using a dislocation filtering layer for ultraviolet light-emitting diodes," CrystEngComm **21**, 4072–4078 (2019).
41. X. Yi, Q.-F. Yang, K. Y. Yang, and K. Vahala, "Theory and measurement of the soliton self-frequency shift and efficiency in optical microcavities," Opt. Lett. **41**, 3419–3422 (2016).
42. M. Karpov, H. Guo, A. Kordts, V. Brasch, M. H. P. Pfeiffer, M. Zervas, M. Geiselmann, and T. J. Kippenberg, "Raman self-frequency shift of dissipative Kerr solitons in an optical microresonator," Phys. Rev. Lett. **116**, 103902 (2016).
43. X. Yi, Q. F. Yang, X. Zhang, K. Y. Yang, X. Li, and K. Vahala, "Single-mode dispersive waves and soliton microcomb dynamics," Nat. Commun. **8**, 14869 (2017).
44. J. Liu, A. S. Raja, M. Karpov, B. Ghadiani, M. H. P. Pfeiffer, B. Du, N. J. Engelsen, H. Guo, M. Zervas, and T. J. Kippenberg, "Ultralow-power chip-based soliton microcombs for photonic integration," Optica **5**, 1347–1353 (2018).
45. B. Shen, L. Chang, J. Liu, H. Wang, Q.-F. Yang, C. Xiang, R. N. Wang, J. He, T. Liu, W. Xie, J. Guo, D. Kinghorn, L. Wu, Q.-X. Ji, T. J. Kippenberg, K. Vahala, and J. E. Bowers, "Integrated turnkey soliton microcombs," Nature **582**, 365–369 (2020).
46. X. Liu, Z. Gong, A. W. Bruch, J. B. Surya, J. Lu, and H. X. Tang, "III-Nitride nanophotonics for beyond-octave soliton generation and self-referencing," arXiv:2012.13496 (2020).